

Studies on crystal growth, vibrational, dielectric, electronic, mechanical and thermal properties of new organic nonlinear optical crystal: 3-nitrocinnamic acid[†]

Cite this: *CrystEngComm*, 2013, 15, 9176

S. Alen,^{ab} D. Sajan,^{*b} K. Job Sabu,^b K. Udaya Lakshmi,^c V. Veeraiah,^d K. Chaitanya^e and V. Bena Jothy^a

3-Nitrocinnamic acid (3NCA) was synthesized and its crystals were grown in aqueous solution by slow evaporation solution growth technique. The grown crystal was confirmed by powder XRD studies. The geometry, intermolecular hydrogen bonding, and harmonic vibrational wavenumbers of 3NCA were investigated with the help of B3LYP density functional theory (DFT) methods. The calculated molecular geometry has been compared with the experimental data obtained from XRD data. The assignments of the vibrational spectra have been carried out with the aid of normal coordinate analysis (NCA) following the scaled quantum mechanical force field methodology (SQMFF). Vibrational spectral investigation confirms the formation of cyclic dimers in the crystal, with the carboxyl groups of each acid molecule bonded to those of adjacent molecules. The red shift of the O–H stretching wavenumber is due to the formation of strong O–H \cdots O hydrogen bonds by hyperconjugation between the carbonyl oxygen lone electron pairs and the O–H σ^* antibonding orbitals. Thermal stability of the grown crystal was examined by recording TGA/DTA. Mechanical strength of the grown material was tested by hardness studies. Second harmonic frequency generation was examined by Kurtz and Perry powder test and it reveals that the relative conversion efficiency is 0.8 times greater than that of urea. The theoretical first order hyperpolarizability value was calculated for the optimized structure.

Received 17th July 2013,
Accepted 6th September 2013

DOI: 10.1039/c3ce41408f

www.rsc.org/crystengcomm

1. Introduction

Cinnamic acid derivatives are an important class of biologically active compounds, playing an important role in the plants' development, but may also present a wide range of actions: antimicrobial, antioxidant, anti-inflammatory, antitumor^{1,2} and nonlinear. The present study investigates the non-linear optical properties of a cinnamic acid derivative, 3-nitrocinnamic acid (NCA) using vibrational spectroscopic techniques. The spectroscopic studies of cinnamic acid and its certain derivatives have been reported earlier.^{3,4}

Nonlinear optical materials have been extensively studied for many years.^{5–9} To design and fabricate NLO materials much effort is being devoted to understand the origin of non-linearity in large systems and to relate NLO responses to electronic structure and molecular geometry. Significant interest still exists in the design and development of materials exhibiting large second-order NLO response because of the potential application in telecommunications, optical computing, optical signal processing, laser technology, data storage and image processing.^{10–15} The design and synthesis of optimized molecules is the key step in this area of research. Recent efforts have been focused on developing organic molecules with large molecular NLO response (β , first hyperpolarizability), improved optical transparency and good thermal stability. It has been found that the β value of molecule can be greatly enhanced by the presence of charge transfer interactions and this principle has been used to identify many highly non-linear molecules.¹⁶ NLO techniques are considered to be among the most structure-sensitive methods to study molecular structures and assemblies. Since the potential of organic materials for NLO devices have been proven, NLO properties of the compounds have been investigated both by experimental and theoretical methods.¹⁷ Vibrational

^a Department of Physics, Women's Christian College, Nagercoil-629001, India.

E-mail: alenstvm@gmail.com (S. Alen), benaezhil@yahoo.com (V. Bena Jothy)

^b Department of Physics, Bishop Moore College, Mavelikara, Alappuzha-690110, Kerala, India. E-mail: dsajand@gmail.com, dsajanbmc@gmail.com

^c Department of Physics, Saveetha School of Engineering, Saveetha University, Thandalam, Chennai 602105D, India. E-mail: udayalakshmi@gmail.com

^d Department of Physics, D.N.R. College (A), Bhimavaram, W.G.D.T.A. P., India-534202. E-mail: avruavru@gmail.com

^e Department of Chemistry, Nanjing University of Science and Technology, Xialingwei 200, Nanjing, People's Republic of China. E-mail: cskcmil@gmail.com

[†] Electronic supplementary information (ESI) available. See DOI: 10.1039/c3ce41408f

spectroscopy has been recently employed to investigate the structural features responsible for the NLO properties. The efforts toward deeper knowledge about the relationships between molecular architecture, nonlinear response, and hyperpolarizability, using vibrational spectra of the molecules, can lead to discovery of new efficient materials for technological applications. The present work deals with growth and detailed vibrational spectral investigation of the crystal 3-nitrocinnamic acid (3NCA) to elucidate the correlation between the molecular structure and NLO property, charge transfer interactions, and first hyperpolarizability, aided by the scaled quantum mechanical force field (SQMFF) technique based on density functional theory (DFT) computation. The UV-visible spectroscopic behavior of 3NCA was investigated in order to predict the electronic properties of the molecule.

The present work describes the growth and vibrational spectral studies on the relationship between the molecular structural features and NLO properties, nonlinear optical response and hyperpolarizability of the push-pull prospective NLO chromophore, 3NCA, with special emphasis on the role of intramolecular charge transfer (ICT) mechanism in such organic materials.

2. Experimental details

2.1. Preparation

The title compound, (3-nitrocinnamic acid), was prepared by dissolving *m*-nitrobenzaldehyde (6 g, 0.04 mol) and malonic acid (8.3 g, 0.08 mol) in a mixture of 5 ml of pyridine and 0.25 ml of piperidine. The solution was allowed to reflux for 1 h, with rapid evolution of CO₂. The resulting title compound was recrystallized from ethanol. The grown crystal is shown in Fig. S1 (ESI).†

2.2. IR, Raman and UV measurements

The FT-IR spectrum of the synthesized material was recorded in the wavenumber range 400–4000 cm⁻¹ by KBr pellet technique (Thermo Nicolet AVATAR 370 DTGS FT-IR spectrophotometer). The NIR-FT-Raman spectra were recorded using a Bruker RFS 100/S spectrometer. The measurements were carried out in the range of 100–3700 cm⁻¹ (Happ-Genzel apodization, 2 cm⁻¹ resolution, 1064 nm Nd:YAG laser excitation, 450 mW power at the sample). The UV-Vis absorption spectrum of the sample was recorded in ethanol solution using a Shimadzu UV-Vis spectrophotometer in the spectral region of 200–500 nm. Thermal analysis of 3NCA was carried out using a Perkin Elmer simultaneous thermogravimetric/differential thermal (TGA/DTA) analyzer. The sample was scanned in the temperature range 20–400 °C at a rate of 10 °C min⁻¹ in an inert nitrogen atmosphere. The differential scanning calorimetry measurements were performed on a METTLER-TOLEDO DSC 1 apparatus equipped with a low temperature attachment. Heating and cooling scans were carried out at 5 °C min⁻¹ in the -80 °C–180 °C temperature range. The powdered 3NCA sample weighed 2.92 mg. Aluminum pans were used.

2.3. Second harmonic generation efficiency measurements

The NLO SHG efficiency of 3NCA was measured by the Kurtz-Perry powder SHG method¹⁸ using Q-switched Nd:YAG laser of 1064 nm wavelength. The input laser beam was passed through the sample after reflection from an IR detector. The output from the sample was filtered by an IR filter to eliminate the fundamental and the second harmonic was detected using monochromator and PMT. The second harmonic efficiency of 3NCA was calculated to be 0.8 times that of urea.

3. Crystal structure

Crystals of 3-nitrocinnamic acid (3NCA) belong to the monoclinic system with $a = 3.7756$ (2) Å, $b = 9.4584$ (13) Å, $c = 24.295$ (4) Å, the space group is $P2_1/n$.¹⁹ In the crystal, the independent 3-nitrocinnamic acid molecules are linked by complimentary intermolecular O–H⋯O hydrogen bonds. Atom O₂₀ acts as a hydrogen bond donor to carbonyl atom O₁₉ of another 3-nitrocinnamic acid molecule ($-x + 1, -y - 1, -z$), the D⋯A distance being 2.636(3) Å and the D–H⋯A angle being 169°. This hydrogen bonding interaction leads to the formation of centrosymmetric dimers with a graph set notation of $R_2^2(8)$. The packing diagram exhibits stacking of such dimers along the crystallographic a axis. The molecular packing with intermolecular hydrogen bonding is shown in Fig. S2 (ESI).†

4. Computational details

DFT calculations were carried out using the GAUSSIAN 09 program package.²⁰ All calculations, which include geometry optimizations and vibrational spectra, were performed on isolated systems using the Becke's three parameter B3LYP exchange correlation method²¹ in combination with *cc*/pvdz basis set²² to derive the complete geometry optimizations and normal mode analysis. The optimized geometry corresponding to the minimum on the potential energy surface have been obtained by solving the self-consistent field (SCF) equations iteratively. Harmonic vibrational wavenumbers have been calculated using analytic second derivatives to confirm the convergence to minima on the potential surface and to evaluate the zero-point vibrational energies without imposing any molecular symmetry constraints. It is a well known fact that *ab initio* calculations tend to overestimate the vibrational wavenumber with respect to the experimental ones. This is due to several reasons, for instance, the use of a finite basis set, the incomplete implementation of the electronic correlation and the neglect of anharmonicity effects in the theoretical treatment. To improve the agreement between the predicted and observed wavenumber, the computed harmonic wavenumbers are usually scaled for comparison. In this work the force field was scaled according to the SQM procedure,²³ the Cartesian representation of the force constants were transferred to a nonredundant set of local symmetry coordinates, chosen in accordance to the

recommendations of Pulay *et al.*²⁴ Normal coordinate analysis was performed to obtain full description of the molecular motion pertaining to the normal modes using MOLVIB program version 7.0 written by Sundius.^{25,26} The Raman activities calculated with Gaussian 09 program are converted to relative Raman intensities using the following relationship.

$$I_i = \frac{f(v_0 - \nu_i)^4 S_i}{\nu_i \left[1 - \exp\left(\frac{-h\nu_i}{kT}\right) \right]} \quad (1)$$

where, ν_0 is the exciting wavenumber (in cm^{-1}), ν_i is the vibrational wavenumber of the i^{th} normal mode, h , c and k are universal constants, and f is the suitably chosen common scaling factor for all the peak intensities.²⁷ The second order polarizability or first hyperpolarizability was calculated using B3LYP with cc-pvdz basis set on the basis of the finite-field approach. The components of the first hyperpolarizability can be calculated using the following equation:

$$\beta_i = \beta_{iii} + 1/3 \sum (\beta_{ijj} + \beta_{jij} + \beta_{jji}), i \neq j \quad (2)$$

Using the x , y and z components, and the magnitude of the first hyperpolarizability tensor can be calculated by

$$\beta = (\beta_x^2 + \beta_y^2 + \beta_z^2)^{1/2} \quad (3)$$

The complete equation for calculating the magnitude of first hyper-polarizability from Gaussian '09W output is given as follows:²⁸

$$\beta = [(\beta_{xxx} + \beta_{xyy} + \beta_{xzz})^2 + (\beta_{yyy} + \beta_{yzz} + \beta_{yxx})^2 + (\beta_{zzz} + \beta_{zxx} + \beta_{zyy})^2]^{1/2} \quad (4)$$

The components of the static and dynamic hyperpolarizability tensor components of 3NCA and urea molecule are shown in Table 1. The calculated first hyperpolarizability value of urea ($\beta_{\text{total}} = 32$ au) at $\lambda = 1064$ nm is in good agreement with the experimental data obtained from the EFISH (electric-field-induced second harmonic generation) measurement in water solution is $(0.45 \pm 0.12) \times 10^{-30}$ esu,

Table 1 First order hyperpolarizability (β) components of 3NCA and urea (a.u.)

β components	Static ($\lambda = \infty$)		Dynamic ($\lambda = 1064$ nm)	
	3NCA	Urea	3NCA	Urea
β_{xxx}	663	6	944	6
β_{xxy}	245	-1	369	-1
β_{xyy}	-192	16	-263	18
β_{yyy}	-43	1	8	1
β_{xxz}	0	0	0	0
β_{xyz}	0	0	0	0
β_{yyz}	0	0	0	0
β_{xzz}	-1	7	-1	9
β_{yzz}	-5	0	-7	0
β_{zzz}	0	0	0	0
$\beta(\text{total})$	510	29	755	32

which ranges from 0.33×10^{-30} to 0.57×10^{-30} esu (38–66 au).²⁹ This indicates that the first hyperpolarizability value calculated with B3LYP/cc-pvdz level agrees well with the experimental. Therefore our calculated results show that the static and dynamic first hyperpolarizability values of 3NCA are nearly 18 and 24 times larger than those of urea.

Geometrical parameters obtained from DFT calculation were used to perform NBO analysis by the NBO 3.1 program³⁰ implemented in Gaussian 09 at DFT/B3LYP level in order to understand various second order interactions between the filled orbital of another subsystem, which is a measure of the delocalization or hyperconjugation. The hyperconjugation interaction energy was deduced from the second-order perturbation approach:

$$E(2) = -n_\sigma \frac{\langle \sigma | F | \sigma \rangle^2}{\varepsilon_{\sigma^*} - \varepsilon_\sigma} = -n_\sigma \frac{F_{ij}^2}{\Delta E} \quad (5)$$

where $\langle \sigma | F | \sigma \rangle^2$ or F_{ij}^2 is the Fock matrix element between i and j NBO orbitals, ε_σ and ε_{σ^*} are the energies of σ and σ^* NBO's and n_σ is the population of the donor σ orbital.

The TD-DFT method was used to calculate energies, oscillator strengths of electronic singlet-singlet transitions and the absorption wavelengths. Solvent effects were considered using the polarizable continuum model (PCM) developed by Tomasi and co-workers.^{31–33}

5. Optimized geometry

The optimized structural parameters of 3NCA for are given in Table S1 (ESI).† The corresponding values from X-ray diffraction are also given in the table for comparison. The optimized molecular structure of the compound with atom numbering scheme adopted in the computations is shown in Fig. 1 (a) and (b) (monomer & dimer, respectively) with Cartesian axes. From the table it can be seen that there are some deviations in the computed geometrical parameters from those reported in the XRD data¹⁹ and these differences are probably due to the intermolecular interactions in the crystalline state. The experimental values of the C–H bond lengths are around 0.94 Å. The interesting structural features of 3NCA are the shortening of endocyclic angle $C_9-C_1-C_2$ at the junction of the phenyl ring and propenoate group and increase of the two neighbouring angle around the ring $C_1-C_9-C_7$ and $C_1-C_2-C_4$ resulting from the charge transfer

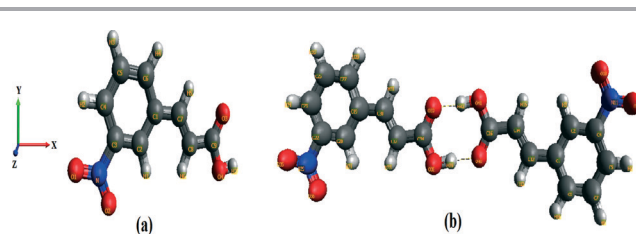


Fig. 1 Optimized structure of 3NCA (a) monomer (b) dimer.

(CT) interaction of the phenyl ring and ester group through C₁₂-C₁₄ double bond. The evidence of such interaction can be inferred from XRD data.¹⁹ DFT calculation indicates an increase of the angles C₁-C₉-C₇ and C₁-C₂-C₄ by 1.41° and 0.5°, respectively, and a reduction in endocyclic angle C₉-C₁-C₂ by 1.76°, associated with the CT interaction. The repulsion between H₃ and H₁₅ leads to the enlargement of angles C₂-C₁-C₁₂ and C₁-C₁₂-C₁₄ by 2.75° and 7.51°, respectively, from 120°. The C₁-C₁₂-C₁₄-C₁₆ torsion angle of -179.9° indicates that the benzene ring and the carboxylic acid group are in an *E* configuration about the C₁₂-C₁₄ bond and the propenoic acid moiety exists in an extended conformation. The dihedral angle between the 3-nitro group and the benzene ring is 8.9°. In a related structure, *viz.* *p*-nitrocinnamic acid,³⁴ the nitro group is coplanar (2.2°) with the benzene ring. With respect to the plane of the benzene ring, the 3-nitro group is oriented at an angle of 45.3° in 4-dimethylamino-3-nitrocinnamic acid,³⁵ 3.6° in 3,5-dinitrocinnamic acid and 2.3° in the 3,5 dinitrocinnamic acid 2,5-dimethoxycinnamic acid complex,³⁶ 3.0° in the 3,5-dinitrocinnamic acid 4-(*N,N*-dimethylamino)benzoic acid complex and 6.1° in the 3,5 dinitrocinnamic acid 4-(*N,N*-dimethylamino)cinnamic acid complex.³⁷

6. Natural bond orbital analysis

Natural bond orbital (NBO) analysis provides an efficient method for studying intra- and intermolecular bonding and charge transfer or conjugative interaction in molecular systems. The NBO analysis allows us to estimate the energy of

the molecule with the same geometry but in the absence of electronic delocalization. The most important interaction between “filled” (donor) Lewis type NBOs and “empty” (acceptor) non-Lewis NBOs is reported in Table 2. The hyperconjugative interactions are formed by the orbital overlap between $\pi(\text{C}-\text{C})$ bond orbital and $\pi^*(\text{C}-\text{C})$ antibonding orbital, which results in intramolecular charge transfer (ICT) causing stabilization of the system. This strong ICT is one of the causes of the NLO activity. These interactions are observed as an increase in electron density (ED) in the C-C antibonding orbital, which weakens the respective bonds. In the benzene ring the ED at the two conjugated π bond (~1.63 e) and π^* bond (~0.3 e) clearly demonstrates the strong delocalization. The strong delocalization of π electron in the benzene ring leads to a stabilization of ~22.5 kcal mol⁻¹. The NBO analysis can be employed to identify and substantiate the possible intra and intermolecular interactions that would form the hydrogen bonded network.³⁸ The existence of intermolecular O-H...O hydrogen bonds, due to the interaction between the lone pair (LP) of oxygen with the antibonding orbital σ^* , has been confirmed by the results of NBO analysis. The energy contribution of LP₁O₄₀ → $\sigma^*(\text{O}_{38}-\text{H}_{39})$, LP₂O₄₀ → $\sigma^*(\text{O}_{38}-\text{H}_{39})$, LP₁O₃₇ → $\sigma^*(\text{O}_{41}-\text{H}_{42})$, LP₂O₃₇ → $\sigma^*(\text{O}_{41}-\text{H}_{42})$ values are 11.10 kcal mol⁻¹, 28.42 kcal mol⁻¹, 11.10 kcal mol⁻¹ and 28.41 kcal mol⁻¹, respectively. These energy $E(2)$ values are chemically significant and can be used as a measure of the intermolecular O-H-O hydrogen bonding interaction between the oxygen lone pair and the antibonding orbitals. The strengthening and contraction of the C-H bonds is due to rehybridization,³⁹ which is revealed by the

Table 2 Second-order perturbation theory analysis of Fock matrix in NBO basis

Donor (<i>i</i>)	ED(<i>i</i>) (e)	Acceptor (<i>j</i>)	ED(<i>j</i>)(e)	$E(2)^a$ (kcal/mol)	$E(j) - E(i)^b$ (a.u.)	$F(i,j)^c$ (a.u.)
$\pi(\text{C}_1-\text{C}_9)$	1.60343	$\pi^*(\text{C}_2-\text{C}_4)$	0.34146	22.33	0.28	0.071
$\pi(\text{C}_1-\text{C}_9)$	1.60343	$\pi^*(\text{C}_5-\text{C}_7)$	0.29661	18.61	0.28	0.066
$\pi(\text{C}_2-\text{C}_4)$	1.66169	$\pi^*(\text{C}_1-\text{C}_9)$	0.35964	17.01	0.30	0.064
$\pi(\text{C}_2-\text{C}_4)$	1.66169	$\pi^*(\text{C}_5-\text{C}_7)$	0.29661	20.71	0.30	0.071
$\pi(\text{C}_5-\text{C}_7)$	1.63859	$\pi^*(\text{C}_1-\text{C}_9)$	0.35964	22.51	0.29	0.072
$\pi(\text{C}_5-\text{C}_7)$	1.63859	$\pi^*(\text{C}_2-\text{C}_4)$	0.34146	20.13	0.28	0.068
$\pi(\text{C}_1-\text{C}_9)$	1.60343	$\pi^*(\text{C}_{12}-\text{C}_{14})$	0.09197	16.00	0.30	0.067
$\pi(\text{C}_2-\text{C}_4)$	1.66169	$\pi^*(\text{N}_{11}-\text{O}_{17})$	0.61854	25.11	0.15	0.060
$\pi(\text{C}_{12}-\text{C}_{14})$	1.85166	$\pi^*(\text{C}_1-\text{C}_9)$	0.35964	11.96	0.30	0.057
$\pi(\text{C}_{12}-\text{C}_{14})$	1.85166	$\pi^*(\text{C}_{16}-\text{O}_{40})$	0.33110	21.48	0.28	0.072
$\pi^*(\text{C}_1-\text{C}_9)$	0.35964	$\pi^*(\text{C}_{12}-\text{C}_{14})$	0.09197	61.30	0.02	0.065
$\sigma(\text{C}_1-\text{C}_{12})$	1.97389	$\sigma^*(\text{C}_{12}-\text{H}_{13})$	0.01869	0.52	1.12	0.022
$\sigma(\text{C}_{16}-\text{O}_{40})$	1.99640	$\sigma^*(\text{C}_{14}-\text{H}_{15})$	0.01702	0.96	1.50	0.034
$\sigma(\text{C}_{19}-\text{C}_{30})$	1.97389	$\sigma^*(\text{C}_{30}-\text{H}_{31})$	0.01869	0.52	1.12	0.022
$\sigma(\text{C}_{34}-\text{O}_{37})$	1.99640	$\sigma^*(\text{C}_{32}-\text{H}_{33})$	0.01702	0.96	1.50	0.034
LP(2)O ₁₇	1.89512	$\sigma^*(\text{N}_{11}-\text{O}_{18})$	0.05643	19.16	0.72	0.106
LP(2)O ₁₈	1.89429	$\sigma^*(\text{N}_{11}-\text{O}_{17})$	0.05616	19.16	0.72	0.107
LP(2)O ₄₀	1.83920	$\sigma^*(\text{C}_{14}-\text{C}_{16})$	0.05355	16.25	0.78	0.103
LP(2)O ₄₀	1.83920	$\sigma^*(\text{C}_{16}-\text{O}_{41})$	0.07064	16.47	0.73	0.100
LP(2)O ₄₁	1.75184	$\pi^*(\text{C}_{16}-\text{O}_{40})$	0.33110	61.93	0.31	0.126
LP(1)O ₄₀	1.94747	$\sigma^*(\text{O}_{38}-\text{H}_{39})$	0.08824	11.10	1.04	0.097
LP(2)O ₄₀	1.83920	$\sigma^*(\text{O}_{38}-\text{H}_{39})$	0.08824	28.42	0.71	0.129
LP(1)O ₃₇	1.94748	$\sigma^*(\text{O}_{41}-\text{H}_{42})$	0.08821	11.10	1.04	0.097
LP(2)O ₃₇	1.83922	$\sigma^*(\text{O}_{41}-\text{H}_{42})$	0.08821	28.41	0.71	0.129

^a $E(2)$ means energy of hyperconjugative interactions; *cf.* eqn (5). ^b Energy difference between donor and acceptor *i* and *j* NBO orbitals. ^c $F(i,j)$ is the Fock matrix element between *i* and *j* NBO orbitals.

low value of electron density (0.01869 e, 0.01702 e, 0.01869 e and 0.01702 e) in the σ^* ($C_{12}-H_{13}$), σ^* ($C_{14}-H_{15}$), σ^* ($C_{30}-H_{31}$) and σ^* ($C_{32}-H_{33}$) orbitals, respectively.

7. UV-Visible spectral studies

In an attempt to understand the nature of electronic transitions in terms of their energies and oscillator strengths, time-dependent DFT (TD-DFT) calculations involving configuration interaction between the singly excited electronic states were conducted on the molecule. The position and absorbance of the experimental peaks together with the calculated excitation energies, oscillator strength (f), wavelength (λ), and spectral assignments are given in Table S2.† The observed and simulated (in gas phase and ethanol) UV-vis spectra are shown in Fig. 2. TD-DFT calculations predict a transition in the near ultraviolet region for 3NCA molecule. The transition at 279 (0.0212) nm, calculated in ethanol using BH and HLYP functional, has been observed at 261 nm and is assigned to $\pi-\pi^*$ transition. The number in parentheses represents oscillator strengths. On the basis of TD-DFT calculations, this shift may be explained as arising out of a larger decrease in the energy of the LUMO orbital (-0.09877 a.u.) than the HOMO (-0.26308 a.u.) relative to its position in 3NCA molecule.

8. HOMO–LUMO analysis

There are lot of applications available for the use of the highest occupied molecular orbital (HOMO) and the lowest unoccupied molecular orbital (LUMO) energy gap as a quantum chemical descriptor. It establishes correlation in various chemical and biochemical systems.^{40,41} For conjugated molecules there is a small separation between HOMO and LUMO. This is the result of a significant degree of ICT from the electron-donor groups to the electron-acceptor groups through a π -conjugated path. The HOMO–LUMO energy gap of 3NCA was calculated at the B3LYP/cc-pvdz level. The HOMO and LUMO orbitals are shown in Fig 3(a) and (b). The energies of

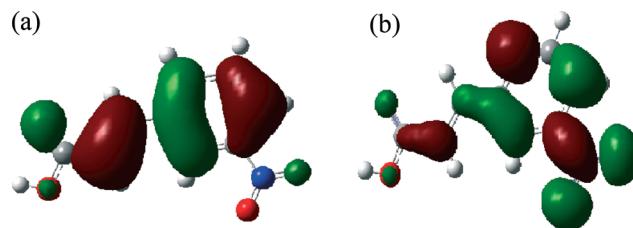


Fig. 3 (a) HOMO plot of 3NCA, (b) LUMO plot of 3NCA.

the HOMO and LUMO, based on the optimized structure, are computed as -0.26308 a.u. and -0.09877 a.u., respectively. The HOMO–LUMO energy gap is -0.16431 a.u. The decrease in the HOMO and LUMO energy gap explains the eventual charge transfer interactions taking place within the molecule as well as the large stabilization of LUMO due to the strong electron-acceptor ability of the electron acceptor group.⁴²

9. Differential scanning calorimetry (DSC) measurements

The DSC thermograms for the 3NCA crystal are shown in Fig. 4. A very sharp and intense endothermic peak at 268.58 °C corresponding to the melting of 3NCA is seen. The temperature range of this phenomenon was constant in comparison to other thermal transitions.⁴³ The phenomenon disappears systematically after a heating–cooling–heating sequence. A glass transition 168.83 °C is seen often linked with a relaxation effect, the amplitude of which depends on the thermal history of the samples. When a material is not sufficiently ordered to crystallize, a glass transition can generally be observed at low temperature. Thus, amorphous material can be characterized by their glass transition temperature (T_g). The glass transition temperature is characterized by a change in heat capacity, which induces a change in the baseline of the thermo analytical DSC curve.

10. Vibrational spectral analysis

The assignment of fundamentals has been made based on normal coordinate analysis following a force field calculation with the same *ab initio* method that was employed for the

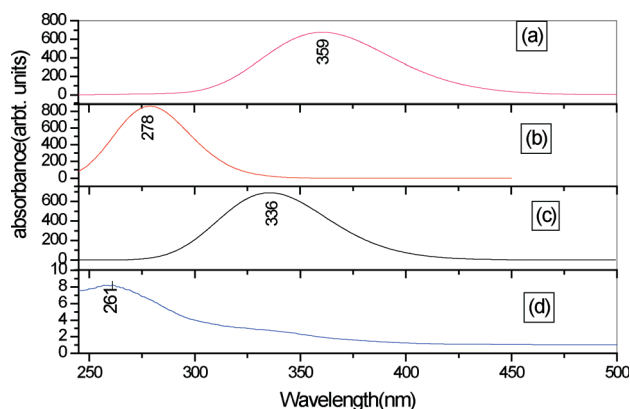


Fig. 2 (a) Simulated UV-vis spectrum of 3NCA in ethanol using B3LYP/6-31G(d), (b) simulated UV-vis spectrum of 3NCA in ethanol using BH and HLYP/cc-pvdz, (c) simulated UV-vis spectrum of 3NCA in gas phase and (d) experimental UV-vis spectrum of 3NCA in ethanol.

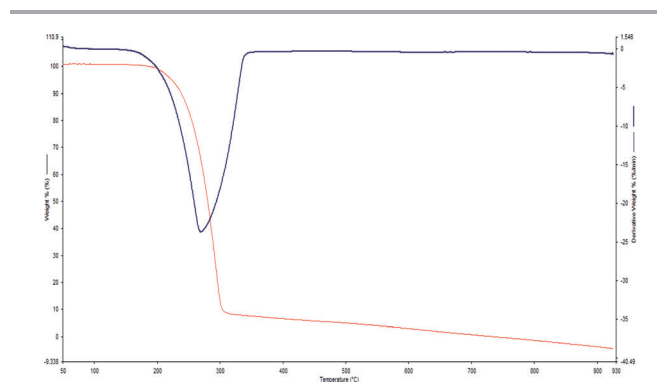


Fig. 4 DSC curve for 3NCA.

geometry optimization of the centrosymmetric dimer molecule. The non-redundant set of internal coordinates for 3NCA dimer has been defined in Table S3,[†] similar to the ‘natural coordinates’ recommended by Pulay *et al.*²⁴ The ‘virtual bond’ coordinates listed in Table S3[†] were used to express the bend and torsion motions of the H-bonded ring of the dimer, as described in the butyrolactam dimer example given by Pulay and coworkers.⁴⁴ In addition, the selective scaling was incorporated according to the SQM scheme using a set of 12 transferable scale factors (given in the fourth column of Table S4[†]) recommended by Rauhut and Pulay⁴⁵ with the RMS frequency error 12.5 cm⁻¹. The SQM wavenumbers related to the observed peaks are presented in Table 3 (infrared active modes & Raman active modes) along with detailed assignments showing symmetry species under *C*_{2h} point group. The observed FT-IR and FT-Raman spectra and simulated theoretical spectra calculated at B3LYP/cc-pvdz level are given in Fig. 5(a) (3750–2000 cm⁻¹) & (b) (2000–400 cm⁻¹) and Fig. 6 for

visual comparison. The DFT calculation shows that the 3NCA monomer and dimer have similar vibrational contributions except that associated with intermolecular O–H···O hydrogen bonds owing to their spectral equivalence. While comparing the IR and Raman spectra, it is found that most of the IR active bands are either weak or inactive in Raman and *vice versa* due to possession of center of symmetry in 3NCA dimer. The symmetry species under *C*_{2h} point group clearly demonstrates mutual exclusion between the IR and Raman spectra and their corresponding activities provide a better approximation to the IR and Raman spectra observed in polycrystalline solid state. The assignments of wavenumbers for the different functional groups are discussed below.

10.1. Phenyl ring vibration

Various normal modes of vibration of the substituted phenyl ring have been comprehensively studied according to

Table 3 Vibrational assignment of 3NCA dimer by normal mode analysis based on SQM force field calculations^d

Experimental wavenumbers (cm ⁻¹)		Scaled wavenumbers (cm ⁻¹)	IR intensity ^a	Raman intensity ^b	Characterization of normal modes with PED ^c (%)
IR	Raman				
3091 m	3091 sh	3103	0.0020	2.42	2 VCH (99)
		3099	0.0020	1.88	7a VCH (99)
	3081 w	3099	0.0020	1.88	7a VCH (99)
		3068	0.0033	3.41	20b VCH (99)
3048 w	3043 w	3068	0.0033	3.41	20b VCH (99)
		3066	0.0032	3.19	13VCH (99)
	3033 w	3033	0.0022	0.844	VCH (99)
		2918	1.0000	0.045	vOH (100)
2977 br		2796	0.0016	18.7	vOH (99)
2876 br		1674	0.0664	1.28	vCO2as (37), bCOH (24), boHO (10), VCCSUB (10)
1694 s	1667 sh	1674	0.0664	1.28	vCO2as (37), bCOH (24), boHO (10), VCCSUB (10)
1632 s	1642 vs	1628	0.0161	52.1	VCCSUB (39), bCOH (19), vCO2as (12), bCH (11)
1614 m	1615 s	1618	0.0689	78.2	vNO2as (64), VCC (14), bNO2ro (10)
1577 m	1577 w	1562	0.0111	56.6	8bVCC (58), vNO2as (16), bCH (13)
		1562	0.0111	56.6	8b VCC (57), vNO2as (16), bCH (13)
1523 s	1527 m	1537	0.00915	5.49	8a VCC (67), bCH (16), bRasy (10)
1487 m	1490 w	1536	0.00915	5.49	19b VCC (67), bCH (16), bRasy (10)
1438 m	1431 w	1427	0.0142	1.51	bCOH (50), boHO (35)
1418 s		1395	0.00733	5.15	19a VCC (46), bCH (37)
1361 s	1358 s	1353	0.0624	12.5	vNO2ss (65), bNO2tw (14), VCN (13)
1320 s	1321 w	1320	0.1270	1.38	bCOH (35), boHO (32), vCO2ss (12)
1287 m	1287 m	1295	0.0192	1.84	14 VCC (69), bCH (11)
		1268 m	0.00418	0.706	3 bCH (62), VCCSUB (18)
1227 s	1212 s	1226	0.00568	2.07	9b bCH (70)
1177 m	1180 w	1191	0.0239	58.9	bCH (24), VCCSUB (20), vCO2ss (11)
989 m		990	0.00140	1.03	tCCOH (68), boHO (30)
947 m		950	0.00414	5.10	4 tRasy (45), gcH (39)
921 m	925 w	934	0.000784	1.61	5 gcH (71), tRtri (15)
870 m	869 w	892	0.00316	2.56	17a gcH (84), gCO2 (12)
827 m	825 w	817	0.0102	0.957	17b gcH (66), tRtri (14)
806 m		812	0.0137	1.03	bNO2tw (54), VCC (10), bRtri (10)
748 m	755 w	743	0.00267	0.440	6 a tRtri (22), gNO2 (21), gCO2 (18), tRasy (14)
718 s	706 w	716	0.004160	0.303	16b tRasy (26), tRtri (23), gCO2(16), gcH (13), gNO2 (10)
		698	0.003530	0.207	bCO2tw (47), boHO (16)
670 s	666 w	672	0.00167	0.513	16a tRtri (60), tRasy (18)
546 m	548	531	0.00152	0.952	bNO2ro (26), bCO2ro (17), bCN (14), bCCsub (11)

^a Calculated IR intensities. ^b Relative Raman intensities calculated by eqn (1) and normalized to 100. ^c Only PED contributions >10% are listed. ^d Abbreviations: vs – very strong, s – strong, m – medium, w – weak, vw – very weak, br – broad, sh – shoulder, ν – stretching, ss – symmetric stretching, as – asymmetric stretching, R – phenyl ring, b – bending, asy – asymmetric deformation, tri – trigonal deformation, b – inplane bending, t – torsion, g – out of plane bending, W – wagging, bRtri – trigonal ring in-plane bending, bRasy – asymmetric ring in-plane bending, bRsy – symmetric ring in-plane bending, tRtri – trigonal ring torsion, tRasy – asymmetric ring torsion, tRsym – symmetric ring torsion.

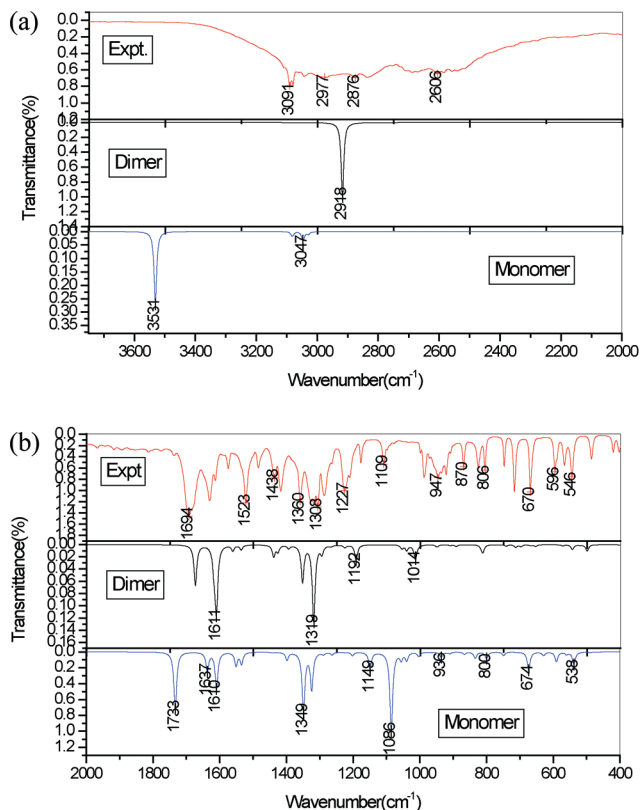


Fig. 5 (a) Experimental and simulated FTIR spectra (3750–2000 cm^{-1}). (b) Experimental and simulated FTIR spectra (2000–400 cm^{-1}).

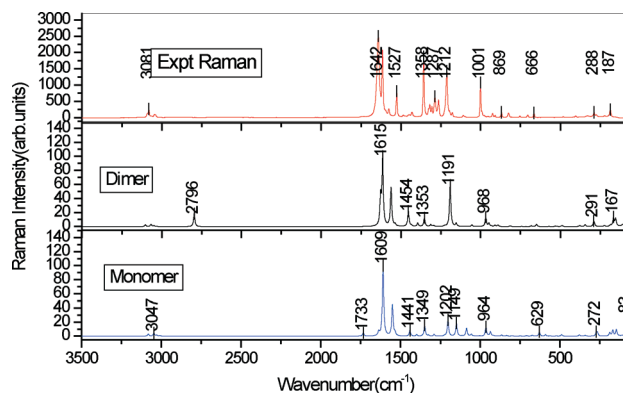


Fig. 6 Experimental and simulated FT Raman spectra.

Wilson's numbering convention.⁴⁶ The selection rule for 1,3-disubstituted benzene derivatives allow four C–H stretching vibrations 2, 7a, 13 and 20b, which are expected in the region 3120–3000 cm^{-1} .^{47,48} But, 13 is absent or is mixed with a very broadband hydroxyl stretch in that region, which cannot be distinctly observed. Mode 2 appears as medium band in IR at 3091 cm^{-1} and at 3091 cm^{-1} in Raman spectrum. The weak band at 3048 cm^{-1} (IR) and a weak band at 3043 cm^{-1} (Raman) are assigned to mode 20b. Mode 7a is observed as a weak band in Raman at 3081 cm^{-1} . The CH stretching modes have been computed at 3103 (PED 99%), 3099 (PED 99%), 3068 (PED 99%) and 3066 (PED 99%) cm^{-1} .

The selection rule allows five normal modes 8a, 8b, 19a, 19b and 14 for the tangential C–C stretching mode in 1,3-disubstituted benzene derivatives. There are two doubly degenerate ring stretching modes e_{2g} (8a, 8b) and e_{1u} (19a, 19b) of benzene which are not perturbed upon substitution. In 1,3-disubstituted benzene the wavenumber of 8a is smaller than that of 8b. DFT computation shows vibrational modes 8a and 8b at 1537 cm^{-1} (PED 58%) and 1562 cm^{-1} (PED 67%); such splitting can be observed experimentally and is allowed for the selection rule for the 1,3-disubstituted ring. The phenyl ring mode 8a manifests as medium band in Raman at 1527 cm^{-1} and strong band in IR at 1523 cm^{-1} and its companion 8b appears as weak and medium band at 1577 cm^{-1} and 1577 cm^{-1} in Raman and IR, respectively. The intensity differences observed between 8a and 8b modes in both IR and Raman spectra is mainly due to the fact that their intensities are dependent on the algebraic difference of the electronic effects of the substituents. The splitting of these modes is due to the generation of two different molecular domains during the intramolecular charge transfer, a partial quinonoid character and one of pure aromatic character, within the π -conjugated system. The 19b mode in 1,3-disubstituted benzene can be expected in the region 1460–1530 cm^{-1} and 19b appears as a medium band between 1370 and 1470 cm^{-1} . The medium IR band observed at 1487 cm^{-1} and weak band at 1490 cm^{-1} correspond to the 19b mode, while the corresponding computed wavenumber is calculated to be 1536 cm^{-1} . The 19a mode appears as a medium band in the IR spectra at 1418 cm^{-1} . The medium band at 1287 cm^{-1} in IR and a medium band at 1287 cm^{-1} in Raman are attributed to mode 14 of C–C stretching. The 8a, 19a and 14 modes appear simultaneously in both IR and Raman spectra, providing evidence for charge transfer interaction,^{49,50} which enables this molecule to be an effective push–pull NLO system.

In 1,3-disubstituted benzene, the phenyl modes 3, 9b, 18a and 18b have been reported to have C–H in-plane bending character and can be expected in the region 1300–1000 cm^{-1} . The C–H in-plane bending vibrations are derived from a_{2g} (1340 cm^{-1}), b_{2u} (1200 cm^{-1}), e_{2g} (1178 cm^{-1}) and e_{1u} (1037 cm^{-1}) modes of benzene. Mode 3 of the in-plane deformation vibrations usually appears at 1264–1300 cm^{-1} . The observed medium band at 1268 cm^{-1} in the Raman spectrum corresponds to the C–H in-plane bending mode 3. The range in which vibration 9a normally appears is 1164–1190 cm^{-1} . The strong IR band identified at 1227 cm^{-1} and strong Raman band at 1212 cm^{-1} can be correlated to the in-plane deformation modes 9a. Further, the 18a mode is generally observed between 1100 and 1128 cm^{-1} . The 18a mode is correlated to the medium band at 1177 cm^{-1} in IR and weak band at 1180 cm^{-1} in Raman. The absorption bands arising from C–H out-of-plane bending vibrations are usually observed in the region 1000–675 cm^{-1} . The out-of-plane vibrations in the benzene arises from b_{2g} (995 cm^{-1}), e_{2u} (975 cm^{-1}), e_{1g} (849 cm^{-1}) and a_{2u} (671 cm^{-1}) modes of benzene. The 17a C–H out-of-plane vibrations are observed as a medium band at 870 cm^{-1} (IR) and weak band at 869 cm^{-1} (Raman) while the medium

IR band 825 cm^{-1} corresponds to mode 17b. Ring mode 5 is identified as a medium IR band at 921 cm^{-1} , which is in good agreement with computational results. The phenyl ring modes 4, 6a, 16b and 16a can be observed in the IR spectrum at 947, 748, 718 and 670 cm^{-1} and the corresponding Raman bands are observed in the same region.

10.2. Vibrations of carboxylic acid group

The O–H stretching band in the IR spectrum of hydrogen-bonded dimer form generally centres around 3000 cm^{-1} and is superimposed on the C–H stretching band.^{47,48,51} 3NCA in the condensed state is characterized by a strongly bonded O–H group (O–H \cdots O = 2.623 Å) with a broad O–H stretching band near 3000 cm^{-1} , which is superimposed on the C–H stretching bands. The broad wings of the O–H stretch can be seen on either side of the C–H bands. In the FT-IR spectrum the broad bands at 2977 cm^{-1} and 2876 cm^{-1} is assigned to O–H stretching vibrations. The hydrogen bonded OH stretching modes for the cyclic dimer of 3NCA were calculated as 2918 cm^{-1} (PED 100%) and 2796 cm^{-1} (PED 99%). By examining the DFT computed values, it is evident that O–H and C=O bonds are significantly elongated, while the C–O bonds are shortened. These results support the formation of strong hydrogen bonded interaction between the O–H \cdots O=C bonds characterized by the elongation of both chemical bonds. The vibrational analysis also supports the above results. The stretching vibrational wavenumber of free O–H is practically unchanged, while that of the bound O–H is red shifted. The red shift of the O–H stretching wavenumber is due to the formation of the strong O–H \cdots O hydrogen bond. Consequently, these bonds become weaker and are elongated and the respective stretching vibrational wavenumbers are red shifted. The red shift of the O–H stretching wavenumber is due to the formation of strong O–H \cdots O hydrogen bonds by hyperconjugation between carbonyl oxygen lone electron pairs and O–H σ^* antibonding orbitals LP (1) $O_{40} \rightarrow \sigma^*(O_{38}\text{--}H_{39})$ & LP (2) $O_{40} \rightarrow \sigma^*(O_{38}\text{--}H_{39})$. This is due to the increase of electron density occurring at C=O σ^* and the antibonding orbitals π^* and O–H σ^* (0.33110 e and 0.088243 e). Consequently, these bonds become weaker and are elongated, and the respective stretching vibrational wavenumbers are red shifted. The perturbation of hyperconjugative interaction charge transfer energies originate from the interaction of the second and first electron lone pairs of carbonyl oxygen (1.83920 e and 1.94747 e) and the O–H σ^* antibonding orbitals (0.08824 e and 0.08821 e).⁵² The broadening in the O–H stretching of 3NCA is due to the combination of bands between the low wavenumber vibrations and $\nu_{\text{O-H}}$ and between the ring vibrations and excited binary combination of δ_{COH} and $\nu_{\text{C-O}}$. The identified two low-wavenumber modes, the in-plane bending and stretching inter-dimer hydrogen-bond modes and the combination bands of $\nu_{\text{C-O}}$, δ_{OH} and $\nu_{\text{C=O}}$ modes may contribute to the shape of ν_{OH} in 3NCA. Thus it may be inferred that this broad ν_{OH} band is indeed a complex one consisting of several sub-bands having different

polarisations. This may be related to the complex structure of the unit cell with two differently oriented molecules, which must give rise to Davydov splitting.

On the low wavenumber wing in the $2700\text{--}2500\text{ cm}^{-1}$ region, there are usually some weaker superimposed shoulder bands attributed to the overtones and combinations of bands near 1420 cm^{-1} and 1300 cm^{-1} (due to O–H bends and C–O stretch) enhanced by Fermi resonance with the broad O–H stretch band.^{47,49,51} The weak bands in the infrared spectrum at 2834 cm^{-1} and 2606 cm^{-1} correspond to overtones and combinations of the 1308 cm^{-1} and 1438 cm^{-1} bands due to interacting C–O stretch and O–H deformation vibrations. These bands result from the Fermi resonance between the proton stretching motions with the bending, in plane proton vibration in their overtone states in the dimers. The Fermi resonance falls just on the activated forbidden transition sub band wavenumber range for the proton stretching vibrations. This resonance seems to belong to the A_g symmetry of the proton vibrational excited state, which is responsible for the longer wavenumber $\nu_{\text{O-H}}$ band branch generation, where the Evans' hole effect used to appear. The $\delta_{\text{O-H}}$ vibrations in their overtone state are also of A_g symmetry and thus Fermi resonance become possible.⁵³ All these facts suggest that a vibronic coupling involving the hydrogen bond protons in the dimers with the π -electrons from aromatic ring systems is responsible for an additional stabilization of the 3NCA dimer. The strong H-bonds linking the two dimers shift the O–H stretch fundamental down into the region where it is in resonance with the overtone and combination bands of the O–H bend and C=O stretch, both of which might be expected to couple strongly to the O–H stretch coordinate. This interaction seems to be responsible for strengthening the anharmonic coupling between the two different proton normal vibrations.

The carbonyl stretching vibrations are found in the region $1780\text{--}1700\text{ cm}^{-1}$.^{47,48,51} The sharp intense band in IR spectrum at 1694 cm^{-1} can be assigned to C=O stretching vibration, which is also observed in the Raman spectrum at 1667 cm^{-1} as a shoulder band. Theoretically the C=O stretching vibrations have been calculated to be 1674 cm^{-1} (PED 37%). The C=O out of plane bending of the 3NCA molecule is observed in the Raman spectrum at 706 cm^{-1} . The C=O in plane bending is observed at 748 cm^{-1} in infrared and at 755 cm^{-1} Raman spectrum. The infrared band for the carboxylic acid dimers is the in phase out of phase O–H \cdots O wagging band^{47,48,51} in the region $990\text{--}875\text{ cm}^{-1}$. This band of medium intensity, noticeably broader than other bands in the vicinity, is also found in 3NCA around at 989 cm^{-1} . The C–O–H in plane bends and C–O stretching modes at 1438 cm^{-1} and 1320 cm^{-1} characteristic of the dimer have also been identified. The increase in wavenumber of this bending mode may be due to their involvement in the O–H \cdots O hydrogen bonding. These bands involve stretching of the C–O bond and in plane deformation of the C–O–H angle, which may interact, so that both bands involve O–H deformation and C–O stretch in and out of phase to some extent. Thus

vibrational spectral investigation confirms formation of cyclic dimers in the crystal with the carboxyl groups of each acid molecule hydrogen bonded to those of adjacent molecules.

10.3. Low wavenumber vibrations of hydrogen bonds

The attractive interaction between the hydrogen donor group and the acceptor moiety leads to the occurrence of new vibrational degrees of freedom, the so called hydrogen bond modes.^{53,54} Such modes are connected with elongations changing the X...Y distance and/or the relative orientation of the hydrogen bonded groups. Thus, they provide direct insight into the structure of hydrogen bonds as well as processes of bond formation and cleavage. As such modes are characterized by a high reduced mass of the oscillator and a small force constant determined by the comparably weak attractive interaction along the hydrogen bond, hydrogen bond modes occur at low wavenumbers in the range between 50–300 cm⁻¹. The low wavenumber bands of the hydrogen bond vibrations are generally found to be weak, broad and asymmetric in the Raman spectrum. The low wavenumber degrees of freedom, such as librations as well as interaction-induced, give rise to additional absorption and Raman bands that frequently overlap with the bands of the hydrogen bond modes. In addition, a substantial spread of vibrational wavenumber occurs for liquids with a multiple hydrogen bonding geometry, resulting in a pronounced inhomogeneous broadening of the vibrational bands. Cyclic dimers of carboxylic acids display a total of six intermonomers, *i.e.*, hydrogen bond modes. Owing to a C₂ symmetry axis perpendicular to the plane of the dimers, three of these modes are Raman active, where the other three are infrared active.⁵⁵ The anharmonic coupling to a single low-wavenumber mode and an intermolecular hydrogen bond stretching mode, together with Davydov coupling, are exclusively responsible for the shape of the O–H stretching bands.⁵⁶ Dimerisation gives rise to six new intermolecular vibrational modes. Because of the C_{2h} inversion symmetry of the acetic acid dimer, three of them are IR active and three are Raman active. Formation of the hydrogen bond gives rise to an enhanced anharmonicity, which entails a strong coupling between the high-wavenumber O–H stretching mode and low-wavenumber modes. Upon coupling of the IR active ν_{OH} mode with the Raman-active low-wavenumber modes, an IR active Franck–Condon series with one or several quanta of low-wavenumber modes arises. The anharmonic coupling of the O–H stretching high-wavenumber mode and low-wavenumber Raman-active modes is identified in 3NCA at 187 and 225 cm⁻¹, respectively, for the hydrogen bond bending (δ_{dimer}) and stretching (ν_{dimer}) modes. The low-wavenumber intermolecular vibrations involving two O–H...O bonds of the dimer at 187 and 225 cm⁻¹ have been attributed to a twist motion of the two molecules involving an in-plane rotation of the molecules against each other, an out-of-plane vibration of the two hydrogen bonds and an antisymmetric dimer stretching mode involving stretching motion along the two hydrogen bonds of the cyclic dimer, respectively.

10.4. Ethylenic group vibrations

The vibrations of the ethylenic bridge are highly sensitive to the degree of charge transfer between the donor and the acceptor groups, hence such stretching modes are of particular interest for spectroscopists. The aliphatic CH stretching bands are expected between 3050 and 3000 cm⁻¹ for cinnamic acid derivatives and the C₁₂–H₁₃ and C₁₄–H₁₅ stretching modes appear at 3033 cm⁻¹ in the Raman spectrum. The in-plane and out-of-plane deformations bands are observed, as expected, in the regions 1510–1000 cm⁻¹ and 1000–750 cm⁻¹, respectively. The alkene bond stretching vibrations in conjugated systems without a center of symmetry interact to produce two C=C stretching bands, near 1650–1600 cm⁻¹. Conjugation of an alkene double bond with an aromatic ring produces enhanced alkene absorption near 1625 cm⁻¹. The absorption bands arising from C=C stretching vibrations are usually observed around 1640 cm⁻¹ for cinnamic acid derivatives.^{49,50} In 3NCA the C₁₂=C₁₄ stretching is observed as an intense band at 1632 cm⁻¹ in the IR spectrum and 1642 cm⁻¹ in the Raman spectrum, whereas the calculated value is 1628 cm⁻¹, PED 39% for the pure C₁₂=C₁₄ stretch. The bands associated with the C₁₂=C₁₄ stretching mode are found to be strongly and simultaneously active in both IR and Raman spectra. Even in the absence of inversion symmetry, in most cases, the strongest bands in the Raman are weak in the infrared and *vice versa*. However the intramolecular charge transfer from the donor to acceptor group through a single–double bond conjugated path can induce large variations of both the molecular dipole moment and molecular polarizability, making IR and Raman activity strong at the same time.^{49,50} Thus in 3NCA, simultaneous infrared and Raman activation of C₁₂=C₁₄ stretching modes clearly points to the charge transfer interaction between –COOH group and phenyl ring through the ethylenic bridge. The π -electron cloud movement from donor to acceptor can make the molecule highly polarized and the intra molecular charge transfer interaction must be responsible for the NLO properties of 3NCA.

10.5. Nitro group vibrations

The nitro group bonded to the phenyl ring (C ϕ NO₂) gives rise to the eight vibrational normal modes. They are described as stretching $\nu_{\text{as}}(\text{NO}_2)$, $\nu_{\text{s}}(\text{NO}_2)$ and $\nu(\phi\text{-NO}_2)$ vibrations and five bending vibrations: $\delta(\text{NO}_2)$, $\omega(\text{NO}_2)$, $\delta(\phi\text{-NO}_2)$ and out-of-plane $\rho(\text{NO}_2)$ and $\gamma(\phi\text{-NO}_2)$. The asymmetric NO₂ vibrations are generally observed in the region 1570–1485 cm⁻¹, while the symmetric stretch will appear between 1370–1320 cm⁻¹.⁵⁷ The most intense band measured at 1614 cm⁻¹ in IR and 1615 cm⁻¹ in Raman can be described as the asymmetric stretching mode of NO₂ group, which is calculated at 1618 cm⁻¹ (64% PED) by the DFT calculations. Since the prop-2-enoic acid groups with aromatic ring are regarded as an efficient electron donor, as reported for similar push–pull NLO systems based on the natural population analysis, the stronger electron acceptor ability of nitro groups may be influenced by the charge differences between donor and acceptor groups of the NLO chromophore.

Further the presence of the strong electron-donating group at the *para* position of the π -conjugated system normally enhances the NO_2 asymmetric stretching intensity to some extent. The blue shifting of the asymmetric stretching mode of NO_2 group and the intensity enhancement may be attributed to the electron-extracting effect of the acceptor groups of the push-pull NLO molecules. The symmetric stretching vibration of NO_2 group is identified as the most intense band at 1361 cm^{-1} in IR and 1358 cm^{-1} in Raman. DFT computations show that this vibration predicted at 1353 cm^{-1} is coupled together with the C-N stretching mode. The large involvement of the NO_2 group in the π -conjugation of this molecule is also evidenced by the strong activity of the band associated to the asymmetric and symmetric stretching vibrations of the nitro group and these vibrations favor the intramolecular charge transfer (ICT) from the donor to the acceptor and gives rise to a large variation of the dipole moment, thus gaining a strong infrared and Raman activity. The nitro group is capable of bending in a number of different directions and these vibrations give rise to several variable intensity bands at low wavenumber. The NO_2 scissoring vibration generally occurs in the range $890\text{--}835\text{ cm}^{-1}$.⁴⁷ The NO_2 scissoring $\delta(\text{NO}_2)$ mode appears at 806 cm^{-1} in IR as a medium band, which is in excellent agreement with the computed results predicted at 812 cm^{-1} . The in-plane NO_2 deformations vibrations have a weak to medium absorption in the region $775\text{--}660\text{ cm}^{-1}$. The symmetric vibrations $\gamma(\text{NO}_2)$ of the out-of-plane deformation (wagging) are identified in the infrared absorption spectra at 750 cm^{-1} and the weak Raman band at 546 cm^{-1} can be correlated to the $\rho(\text{NO}_2)$ vibration (rocking).

11. Microhardness studies

Microhardness studies have been carried out on the polished NCA crystal using Leica, Reichert polyvar 2, MET Vickers microhardness tester fitted with a diamond indenter. The well polished NCA crystal with smooth and dominant face

was placed on the platform on the Vickers microhardness tester. Hardness value on the (011) plane of NCA crystal was estimated for different loads varying from 5–40 g with a step of 5 g for a dwell period of 3 s using Vickers diamond pyramid indenter attached to an incident ray microscope.

The relation between hardness number (H_v) and load (P) for NCA crystal is as shown in Fig. 7 (a). At lower loads the hardness increases gradually with the increase of load and remains constant up to 40 g and above 40 g significant cracks occurred on the smooth surface of the crystal due to release of the internal stress generated locally by indentation. Thus at this point the crack initiation and materials chipping become significant beyond 40 g of the applied load, therefore the hardness test could not be carried out above this load.

Fig. 7(b) shows the plot of logarithmic of load P vs logarithmic of diagonal length of impression. From the slope of the $\log P$ vs $\log d$ plot, the value of n was found to be 3.2, which gives the work hardening index. From the expression $H_v = bP^{(n-2)/n}$, it is inferred that H_v should increase with increase of P if $n > 2$ and decrease if $n < 2$. The calculated value of n for 3NCA crystal agrees well with the experimental value. The indentation mark on the 3NCA crystal for 10 g and 30 g was recorded as shown in Fig. S3 & S4 (ESI).[†] According to Onitsch⁵⁸ and Hanneman,⁵⁹ n should lie between 1 to 1.6 for hard materials and above 1.6 for soft materials.⁶⁰ Thus the grown 3NCA crystal belongs to the soft material category.

The material constant k_1 was calculated using the relation $k_1 = P/d^n$ and it was found to be $3.52 \times 10^{-5}\text{ kg m}^{-1}$. It was also calculated from a graph drawn between P vs. d^n as shown in Fig. S5 (ESI).[†] The slope of the curve gives the value of the material constant k_1 , which was found to be $3.52 \times 10^{-5}\text{ kg m}^{-1}$.

The elastic stiffness constant (C_{11}) was calculated by using Wooster's empirical relation as $C_{11} = H^{7/4}$.⁶¹ The calculated stiffness constant for different loads is listed in Table 4. A graph is plotted against C_{11} versus P as shown in Fig. 8(a).

The resistance pressure is defined as a minimum level of indentation load (W) below which there is no plastic

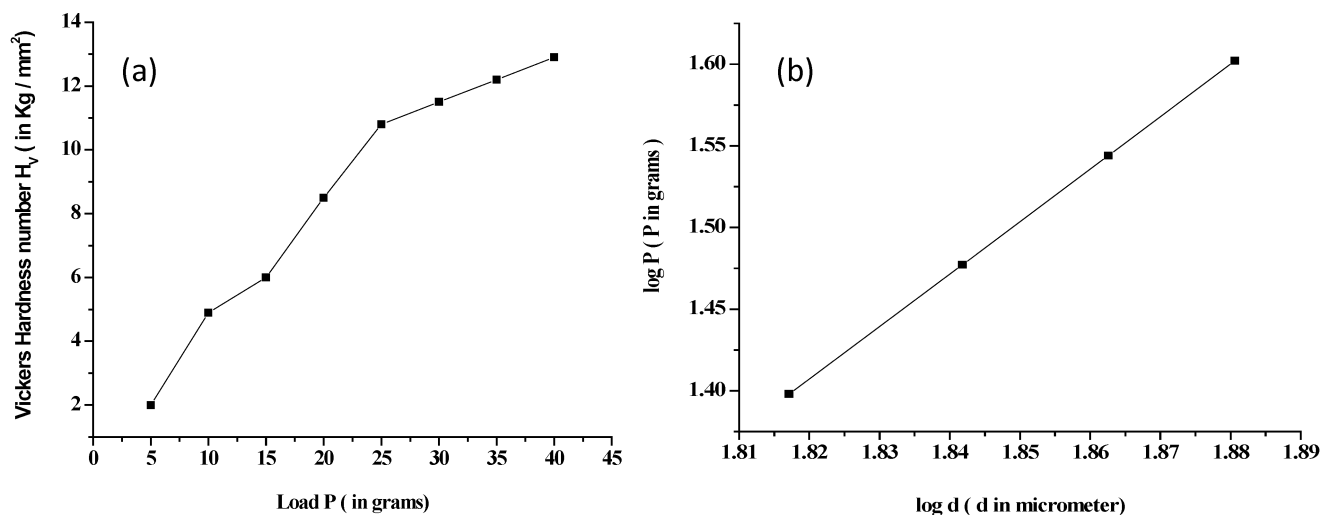


Fig. 7 (a) H_v vs load for NCA, (b) $\log P$ vs $\log d$.

Table 4 Stiffness constant of 3NCA for various load

Load (<i>P</i>) g	Stiffness constant (<i>C</i> ₁₁) kg mm ⁻²	Load (<i>P</i>) g	Stiffness constant (<i>C</i> ₁₁) kg mm ⁻²
5	3.447586841	25	63.95766249
10	16.0264295	30	72.11533616
15	22.83504577	35	79.86303056
20	42.2584297	40	87.27977564

deformation.⁶² Hays and Kendall proposed a relationship to calculate the *W* by the equation

$$d^n = (W/k_1) + (k_2/k_1)d^2 \quad (6)$$

The plot between d^n and d^2 in Fig. 8(b) gives a straight line having slope (k_2/k_1) and intercepts (W/k_1) . From the graph, the slope and intercept were found to be 2.91×10^2 and 6.38×10^5 . From these values, the minimum level of

indentation load *W* was calculated as 22.5 grams and the value of *n* was found to be 3.2. From this analysis, it is clear that below 22.5 grams, the crystal does not exhibit plastic deformation and from 22.5 grams, it exhibits plastic deformation. Beyond 40 g, cracks were developed on the smooth surface of the crystal.

12. Dielectric Studies

The dielectric constant of 3NCA crystals was studied at different temperatures using HIOKI 3532 LCR HITESTER in the frequency region 1000 Hz to 1 MHz. Fig. 9(a) shows the plot of dielectric constant (ϵ_r) vs log frequency for the temperature of 40 °C, 80 °C and 120 °C. The dielectric constant is low at lower temperature and it increases with an increase in temperature sharply up to the Curie point. The dielectric constant has high values in the lower frequency region and then decreases with the applied frequency. The very high value of

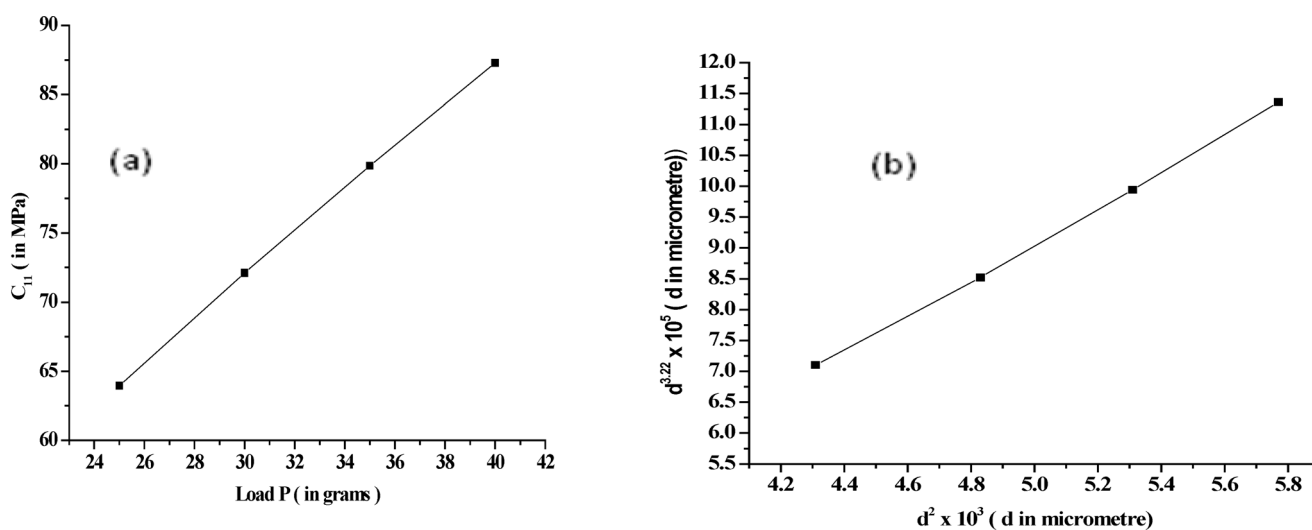


Fig. 8 (a) C_{11} vs *P*, (b) $d^{3.2}$ vs d^2 .

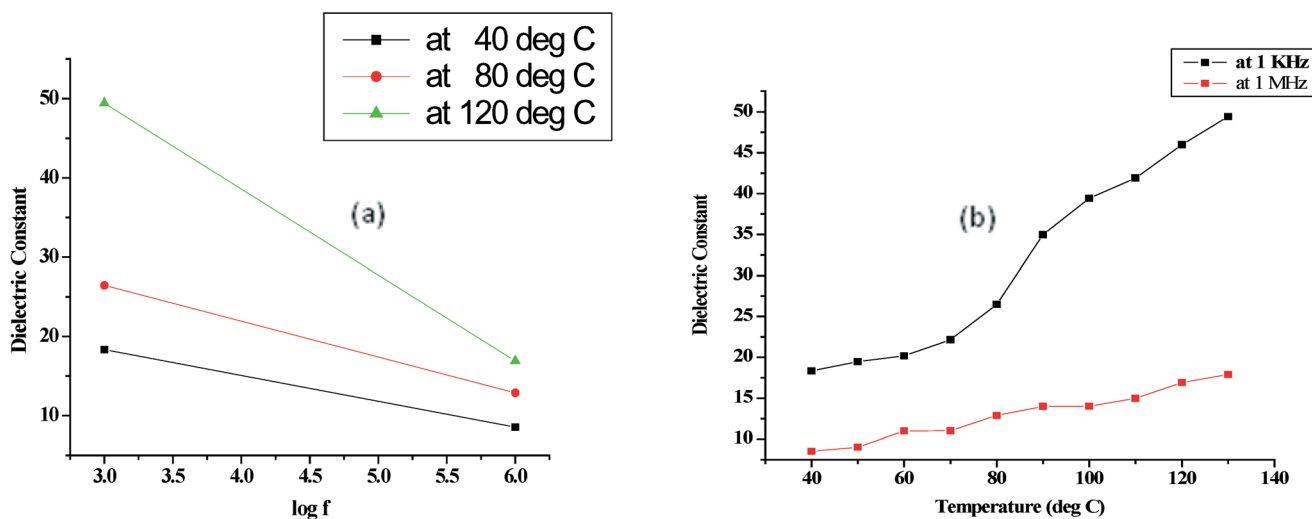


Fig. 9 (a) Dielectric constant vs log *f*, (b) dielectric constant vs temperature.

ϵ_r at low frequencies may be due to the presence of all the four polarizations namely, space charge, orientation, electronic and ionic polarization and its low value at higher frequencies may be due to the loss of significance of these polarizations gradually. Fig. 9(b) shows the temperature dependence of dielectric constant of the 3NCA crystals at frequencies of 1 KHz and 1 MHz. From the plot, it is observed that the dielectric constant increases with increase in temperature, attributed to space charge polarization near the grain boundary interfaces, which depends on the purity and perfection of the crystal. Space charge polarization is generally active at lower frequencies for high temperatures and indicates the perfection of the crystals.⁶³ The low dielectric constant at higher frequencies shows that NCA is a more suitable candidate for NLO applications.

13. Conclusions

The 3NCA crystals were grown by the slow evaporation technique. The calculated first hyperpolarizability is 4.58×10^{-30} e. s.u, which is 18 times that of urea. The normal coordinate analysis performed on 3NCA reproduces its experimental geometry and harmonic vibrational wavenumbers excellently. The red shifting of C–H stretching wavenumber indicates the formation of C–H \cdots O hydrogen bonding. The existence of intermolecular O–H \cdots O hydrogen bonds due to the interaction between the lone pair of oxygen with the antibonding orbital has been confirmed by the results of NBO analysis. The NBO analysis also reveals hyperconjugative interaction, ICT and stabilization of molecules. UV-visible spectral analysis has been carried out. The simultaneous activation of modes 8a, 19a and 14 in both IR and Raman spectra provides evidence for the charge transfer interaction. The vibrational spectral investigation confirms formation of cyclic dimers in the crystal, with the carboxyl groups of each acid molecule hydrogen bonded to those of adjacent molecules. The HOMO–LUMO orbitals clearly explicate the charge transfer interaction taking place within the molecule. The dielectric study shows that NCA is a suitable candidate for NLO applications.

Acknowledgements

D. S. (D. Sajan) thanks the Council of Scientific and Industrial Research (CSIR), New Delhi-110012, India for the financial support (No. 03(1247)/12/EMR-II. The author is highly grateful to Prof. T. Sundius for the Molvib program.

References

- 1 F. M. Da Cunha, D. Duma, J. Assreuy, F. C. Buzzi, R. Niero, M. M. Campos and J. B. Calixto, *Free Radical Res.*, 2004, **38**(11), 1241–1253.
- 2 B. Narasimhan, D. Belsare and D. Pharande, *J. Med. Chem.*, 2004, **39**(10), 827–834.
- 3 M. Kalinowska, R. Jwisiocka and W. Lewandowski, *J. Mol. Struct.*, 2007, **834–836**, 572–580.
- 4 V. Bena Jothy, D. Sajan, C. Ravikumar, I. Némec, C.-N. Xia, V. K. Rastogi and I. Hubert Joe, *J. Raman Spectrosc.*, 2009, **40**, 1822–1830.
- 5 A. Karakas, A. Elmali, H. Unver, H. Kara and Y. Yahsi, *Z. Naturforsch.*, 2006, **61**, 968–974.
- 6 H. Unver, A. Elmali, A. Karakas, H. Kara and E. Donmez, *J. Mol. Struct.*, 2006, **800**, 18–22.
- 7 K. Pedersen, T. G. Pedersen, T. B. Kristensen and P. Morgen, *Appl. Phys. B*, 1999, **68**, 637–640.
- 8 E. A. Perpete, J. M. Andre and B. Champagne, *J. Chem. Phys.*, 1998, **109**, 4624–4638.
- 9 D. M. Bishop, J. M. Luis and B. Kirtman, *J. Chem. Phys.*, 1998, **108**, 1013–1019.
- 10 T. G. Pedersen, K. Pedersen, P. K. Kristensen, J. Rafaelsen, N. Skivesen, Z. Li and S. V. Hoffmann, *Surf. Sci.*, 2002, **516**, 127–133.
- 11 A. Elmali, A. Karakas and H. Unver, *Chem. Phys.*, 2005, **309**, 251–257.
- 12 A. Karakas, H. Unver, A. Elmali and I. Svoboda, *Z. Naturforsch.*, 2005, **60a**, 376–382.
- 13 A. Karakas, A. Elmali, H. Unver and I. Svoboda, *J. Mol. Struct.*, 2004, **702**, 103–110.
- 14 R. Zalesny, W. Bartkowiak, P. Toman and J. Leszczynski, *Chem. Phys.*, 2007, **337**, 77–80.
- 15 P. A. Angelimary and S. Dhanuskodi, *Cryst. Res. Technol.*, 2001, **36**, 1231–1237.
- 16 J. C. Calabrese and S. H. Stevenson, *Chem. Phys. Lett.*, 1989, **154**, 93–96.
- 17 H. S. Nalwa, M. Hanack, G. Pawlowski and M. K. Engel, *Chem. Phys.*, 1999, **245**, 17–26.
- 18 S. K. Kurtz and T. T. Perry, *J. Appl. Phys.*, 1968, **39**, 3798.
- 19 K. Udaya Lakshmi, S. Thamotharan, M. Srinivasan, K. Ramamurthi and B. Varghese, *Acta Crystallogr., Sect. E: Struct. Rep. Online*, 2005, **61**, o3636–o3638.
- 20 M. J. Frisch, G. W. Trucks, H. B. Schlegel, G. E. Scuseria, M. A. Robb, J. R. Cheeseman, J. A. Montgomery Jr., T. Vreven, K. N. Kudin, J. C. Burant, J. M. Millam, Iyengar, J. Tomasi, V. Barone, B. Mennucci, M. Cossi, G. Scalmani, N. Rega, G. A. Petersson, H. Nakatsuji, M. Hada, M. Ehara, K. Toyota, R. Fukuda, J. Hasegawa, M. Ishida, T. Nakajima, Y. Honda, O. Kitao, H. Nakai, M. Klene, X. Li, J. E. Knox, H. P. Hratchian, J. B. Cross, V. Bakken, C. Adamo, J. Jaramillo, R. Gomperts, R. E. Stratmann, O. Yazyev, A. J. Austin, R. Cammi, C. Pomelli, J. W. Ochterski, P. Y. Ayala, K. Morokuma, G. A. Voth, P. Salvador, J. J. Dannenberg, V. G. Zakrzewski, S. Dapprich, A. D. Daniels, M. C. Strain, O. Farkas, D. K. Malick, A. D. Rabuck, K. Raghavachari, J. B. Foresman, J. V. Ortiz, Q. Cui, A. G. Baboul, S. Clifford, J. Cioslowski, B. B. Stefanov, G. Liu, A. Liashenko, P. Piskorz, I. Komaromi, R. L. Martin, D. J. Fox, T. Keith, M. A. Al-Laham, C. Y. Peng, A. Nanayakkara, M. Challacombe, P. M. W. Gill, B. Johnson, W. Chen, M. W. Wong, C. Gonzalez and J. A. Pople, *Gaussian 09, Revision B.01*, Gaussian, Inc., Wallingford, C.T., 2010.
- 21 A. D. Becke, *J. Chem. Phys.*, 1999, **98**, 5648–5652.
- 22 T. H. Dunning Jr., *J. Chem. Phys.*, 1989, **90**(2), 1007–1023.

- 23 J. Baker, A. A. Jarzecki and P. Pulay, *J. Phys. Chem.*, 1998, **102**, 1412–1424.
- 24 P. Pulay, G. Fogarasi, F. Pang and J. E. Boggs, *J. Am. Chem. Soc.*, 1979, **101**, 2550–2560.
- 25 T. Sundius, *J. Mol. Struct.*, 1990, **218**, 321–326.
- 26 T. Sundius, *Vib. Spectrosc.*, 2002, **29**, 89–95.
- 27 G. Keresztury, S. Holly, J. Varga, G. Besenyei, A. Y. Wang and J. R. Dearing, *Spectrochim. Acta, Part A*, 1993, **49**, 2007–2019.
- 28 K. S. Thanthiriwatte and K. M. Nalin de Silva, *J. Mol. Struct.: THEOCHEM*, 2002, **617**, 169–175.
- 29 I. Ledoux and J. Zyss, *Chem. Phys.*, 1982, **73**, 203–213.
- 30 E. D. Glendening, A. E. Reed, J. E. Carpenter and F. Weinhold, NBO Version 3.1, TCI, University of Wisconsin, Madison, 1998.
- 31 S. Miertus, E. Scrocc and J. Tomasi, *Chem. Phys.*, 1981, **55**, 117–129.
- 32 S. Miertus and J. Tomasi, *Chem. Phys.*, 1982, **65**, 239–245.
- 33 M. Cossi, V. Barone, R. Cammi and J. Tomasi, *Chem. Phys. Lett.*, 1996, **255**, 327.
- 34 Y. Kageyama, T. Iwamoto, M. Haisa and S. Kashino, *Acta Crystallogr., Sect. C: Cryst. Struct. Commun.*, 1993, **49**, 833–834.
- 35 C. P. Huber, *Acta Crystallogr., Sect. C: Cryst. Struct. Commun.*, 1985, **41**, 1076–1079.
- 36 G. R. Desiraju and C. V. K. Sharma, *J. Chem. Soc. Chem. Commun.*, 1991, 1239–1241, DOI: 10.1039/C39910001239.
- 37 C. V. K. Sharma, K. Panneerselvam, T. Pilati and G. R. Desiraju, *J. Chem. Soc., Perkin Trans.*, 1993, **2**, 2209–2216.
- 38 M. Montejo, A. Navarero, G. J. Kealey, J. Vazquez and J. J. L. Gonzalez, *J. Am. Chem. Soc.*, 2004, **126**, 15087–15095.
- 39 I. V. Alabugin, M. Manoharan, S. Peabody and F. Weinhold, *J. Am. Chem. Soc.*, 2003, **125**, 5973–5987.
- 40 D. F. V. Lewis, C. Loannides and D. V. Parke, *Xenobiotica*, 1994, **24**, 401–408.
- 41 Z. Zhou and R. G. Parr, *J. Am. Chem. Soc.*, 1990, **112**, 5720–5724.
- 42 L. Padmaja, C. Ravikumar, D. Sajan, I. Hubert Joe, V. S. Jayakumar, G. R. Pettit and O. Faursov Nielsen, *J. Raman Spectrosc.*, 2009, **40**, 419–428.
- 43 M. Giordano, M. Russo, P. Capoluongo, A. Cusano and L. Nicolais, *J. Non-Cryst. Solids*, 2005, **351**, 515–522.
- 44 G. Fogarasi, X. Zhou, P. W. Taylor and P. Pulay, *J. Am. Chem. Soc.*, 1992, **114**, 8191–8201.
- 45 G. Rauhut and P. Pulay, *J. Phys. Chem.*, 1995, **99**, 3093–3100.
- 46 G. Varsanyi, *Assignments for Vibrational Spectra of Seven Hundred Benzene Derivatives*, Adam Hilger, London, vol 1 and vol II, 1974.
- 47 B. Smith, *Infrared Spectral Interpretation: A Systematic Approach*, CRC, Washington, DC, 1999.
- 48 N. B. Colthup, L. H. Daly and S. E. Wiberley, *Introduction to Infrared and Raman Spectroscopy*, Academic Press, New York, 1990.
- 49 D. Sajan, J. Binoy, I. H. Joe, V. S. Jayakumar and J. Zaleski, *J. Raman Spectrosc.*, 2005, **36**, 221–236.
- 50 J. L. Castro, M. R. Lopez Ramirez, I. L. Tocon and J. C. Otero, *J. Raman Spectrosc.*, 2002, **33**, 455–459.
- 51 F. R. Dollish, W. G. Fateley and F. F. Bentley, *Characteristic Raman Frequencies of Organic Compounds*, John Wiley & Sons, New York, 1997.
- 52 J. Chocholousova, V. Spirko and P. Hobza, *Phys. Chem. Chem. Phys.*, 2004, **6**, 37–41.
- 53 J. Dreyer, *Int. J. Quantum Chem.*, 2005, **104**, 782–793.
- 54 E. T. J. Nibbering and T. Elsaesser, *Chem. Rev.*, 2004, **104**, 1087.
- 55 Y. J. Kwon, S. B. Lee, K. Kim and M. S. Kim, *J. Mol. Struct.*, 1994, **318**, 25–35.
- 56 K. Heyne, N. Huse, J. Dreyer, E. T. J. Nibbering and T. Elsaesser, *J. Chem. Phys.*, 2004, **121**, 902–913.
- 57 G. Socrates, *Infrared and Raman Characteristic Group Frequencies, Tables and Charts*, Wiley, Chichester, 2001.
- 58 E. M. Onitsch, *Mikroskopie*, 1998, **95**, 12–14.
- 59 M. Hanneman, *Metall. Manchu*, 1941, **23**, 135.
- 60 R. Ramesh Babu, S. Kumaresan, N. Vijayan, M. Gunasekaran, R. Gopalakrishnan, P. Kannan and P. Ramasamy, *J. Cryst. Growth*, 2003, **256**, 387–392.
- 61 W.A. Wooster, *Rep. Prog. Phys.*, 1953, **16**, 62–82.
- 62 V. Gupta, K. K. Bamzai, P. N. Kotru and B. M. Wanklyn, *Mater. Chem. Phys.*, 2005, **89**, 64–71.
- 63 A. Selvama, S. Pandia, S. Selvakumar and S. Srinivasana, *Arch. Appl. Sci. Res.*, 2012, **4**(6), 2474–2478.